A BCI Framework using Derivative Similarity Metrics to Characterize EEG Spatiotemporal Dynamics with Applications in Neuromarketing

SVETOSLAV KREMENSKI[1], ANNA LEKOVA[2], ADELINA KREMENSKA[1]
[1]Institute of Robotics, Bulgarian Academy of Sciences,
Acad. Georgi Bonchev str. bl.2, 1113 Sofia,
BULGARIA

[2]Institute of Robotics, Bulgarian Academy of Sciences,
Centre of Competence: Intelligent Mechatronic, Eco- And Energy-Saving Systems and Technologies,
Acad. Georgi Bonchev str. bl.2, 1113 Sofia,
BULGARIA

Abstract: - A real-time brain–computer interface (BCI) framework for social robots to predict impulsive decision-making and hidden emotional responses is proposed. A novel neuromarker is defined as sliding-window Pearson correlation of second derivatives of EEG band power across channels within the early reaction interval (0.5-2s). Validated in a neuromarketing pilot study using Furhat robot, the BCI successfully classified participants' intentions to "like", "dislike" or "purchase" advertised products Results showed strong polarity-dependent neural differentiation (inverse correlations, $r < -0.60$), most prominently in the theta band (AF3, F3, C3, AF4, Pz, P4). This dynamic analysis was complemented with effect-size statistical evaluations (Cohen's d). Convergence criteria ($|d| \geq 0.60$) revealed robust neuromarkers primarily in frontal-parietal theta-band electrodes, alongside complementary alpha (F3, Pz, T8, T7) and beta band (Cz, Pz) contributions. These findings demonstrate that the proposed derivative-similarity neuromarker provides a computationally efficient and statistically robust approach for robot-mediated BCI decoding of impulsive evaluative decisions.

Key-Words: - EEG BCI, EEG Spatiotemporal Dynamics, Derivative-Similarity-Driven BCI, Furhat robot, OpenBCI, Node-RED, Neuromarketing.

Received: March 13, 2026. Revised: May 6, 2026. Accepted: June 5, 2026. Published: September 7, 2026.

1 Introduction

EEG signals are characterized by high nonlinearity and temporal non-stationarity, which set significant challenges for feature extraction and classification methods. Classical machine learning techniques (e.g., SVM and kNN), as well as standard statistical approaches (e.g., ANOVA and t-test), fail to capture dynamic changes and the complex interactions between different brain regions. These methods typically rely on static features and linear relationships, which constitutes a limitation when analyzing highly dynamic neurophysiological signals. Standard approaches in EEG analysis include time-frequency methods (e.g., STFT, wavelets, Hilbert transforms) and sliding-window methods (e.g., sliding-window Pearson correlations or cosine shape similarity) to account for the non-stationary nature of EEG signals. These approaches address different scientific issues. Sliding-window correlations are particularly suitable when the goal is to examine time-varying changes in functional connectivity between conditions or to assess whether patterns of activity across channels become synchronized over time. Although short-time Fourier transform and wavelet methods are well-suited for detailed spectral and phase analyses, they are computationally intensive. In contrast, signal derivatives are highly effective at capturing fast neural fluctuations while remaining computationally lightweight, making them an efficient means of detecting neural bursts associated with impulsive choice. However, even when applied in sliding windows, Pearson correlation and cosine similarity capture only linear relationships and cannot reflect fast temporal changes, which may lead to loss of information in the presence of complex oscillatory structures and nonlinear dependencies. To address this limitation, we propose an analysis based on derivatives, either of the time series or of spectral power (P) across different frequency bands, which allows us to capture fine-grained EEG dynamics and reveal structures that remain hidden in the original signals, such as the rate of change of EEG power

and unexpected transitions. Specifically, the second-order derivative reflects the acceleration of oscillations and can highlight changes in curvature, capturing sudden bursts in oscillatory activity. The dynamic use of derivatives of EEG data, particularly second-order derivatives, and their potential as neuromarkers are supported by a few studies, [1], [2].

The proposed approach here applies sliding-window Pearson correlation, which involves computing the Pearson coefficient between two features within a moving time window, providing a time-resolved measure of similarity. Careful selection of the window size is important: if the window is too short, correlations become noisy; if it is too long, temporal resolution is lost. Therefore, we used a 500 ms sliding window with 50% overlap, which is generally considered acceptable and commonly used to approximate local stationarity when computing Pearson correlations in EEG data. This choice aligns with EEG dynamic connectivity studies, [3], which used 500-ms sliding windows with 50% overlap to capture multiple cycles of low-frequency activity (~8Hz) while preserving sensitivity to rapid connectivity changes.

The Pearson correlation coefficient is commonly used in EEG literature to quantify the degree of co-variation between time series recorded from different electrodes or brain regions. It helps researchers assess synchronization, functional connectivity, and shared neural activity patterns across neural sources, [4]. Another commonly used measure in connectivity studies is cosine similarity, which is often used alongside other synchrony metrics such as mutual information and cross-correlation to evaluate synchronization between EEG channels for cognitive task recognition, [5].

To the best of our knowledge, the reported studies do not employ Pearson correlation of second-order temporal derivatives of EEG power as a neuromarker. Furthermore, the Pearson correlation of derivatives captures only structural temporal relationships between signals. It does not measure between-condition mean differences, within-condition variability, trial-to-trial dispersion, or the statistical separability of distributions across participants or trials. To address these distribution-level properties, we additionally computed Cohen's *d* with 95% Confidence Intervals (CIs) for the different conditions.

Therefore, we propose a novel neuromarker based on the Pearson correlation of second-order temporal derivatives of EEG power across frequency bands and electrodes, computed within sliding windows over the impulsive reaction interval (0.5-2.0s). This measure quantifies stimulus-related differences in spatiotemporal power dynamics by assessing the similarity or dissimilarity of curvatures in their temporal profiles. To evaluate statistical separability between the two conditions, the consistency of observed differences across trials, and the practical significance of the effects, we complement this analysis with Cohen's *d*, which quantifies standardized mean differences by considering between-group mean separation, pooled within-group variance, sample size, and statistical uncertainty. Thus, we integrate Pearson-based dynamic measures with effect size statistics and CIs to provide an integrated characterization of both temporal and static neural differentiation. The proposed BCI framework exploits such derivative-based similarity metrics to model the spatiotemporal EEG dynamics underlying impulsive choice behavior. It is lightweight and designed for seamless integration with social robots, enabling immediate adaptive responses to user preferences.

We found no prior work proposing a BCI framework that employs derivative-similarity-based metrics to characterize EEG spatiotemporal dynamics in a neuromarketing context, and that is designed and validated for real-time operation and integration with social robots. This is important because neuromarketing is a marketing research field that examines consumers' cognitive and emotional responses to advertisements, offering an alternative to traditional methods such as interviews, surveys, and focus groups, which may fail to capture true preferences despite the substantial financial investments made in marketing research each year. As an emerging multidisciplinary field, neuromarketing integrates neuroscience, statistics, machine learning, and conventional marketing strategies, including traditional market research methods such as surveys, focus groups, interviews, and observation, as well as the marketing mix framework (the 4 Ps: product, price, place, and promotion). It also encompasses various advertising channels, including print media, broadcast, outdoor, and direct mail, along with sales promotion techniques such as discounts, coupons, loyalty programs, and free samples. By utilizing BCI technology, neuromarketing aims to uncover hidden preferences and purchase intentions in response to marketing stimuli, providing deeper insights into consumer reactions to marketing stimuli. Several neurophysiological findings provide an empirical basis for modeling consumer decision processes using BCI and neuromarketing approaches. These studies identify specific electrodes and frequency bands associated with "like" and "dislike"

preferences. Prior work, [6], [7], [8], demonstrates that EEG activity within these channels and frequency ranges can both predict consumer choices and help interpret neural responses during product evaluation. In particular, frontal electrodes such as AF3, AF4, F3, F4, F7, and F8 are consistently reported as the most informative sites for decoding affective attitudes and purchase intentions in EEG-based neuromarketing studies, [7]. Aggregating signals across frontal channels tends to yield the highest classification accuracy for "like" and purchase decisions, while the distinction between "like" and "dislike" conditions is primarily reflected in differences in temporal dynamics and signal variability rather than in electrode spatial location. According to [7], the most dominant frequency bands for frontal electrodes during purchase intention processing are Theta (4–8 Hz), reflecting cognitive control, evaluation, and decision-making, and Beta (13–32 Hz), contributing to engagement and action readiness. Findings in [8], feature brain activity at the subconscious level and demonstrate the utility of millisecond-precision EEG in investigating early cognitive changes, including preconscious processes.

The goal of this study is to develop a BCI framework for analyzing the spatiotemporal dynamics of EEG activity by examining the second-order temporal derivatives of EEG power across frequency bands and electrodes, computed within sliding windows over the impulsive reaction interval (0.5-2.0s), identifying the most discriminative electrodes, and supporting a robot-mediated BCI system for real-time decision-making and prediction. The proposed framework is validated within a robot-mediated experimental setting to evaluate its effectiveness for neuromarketing research.

The paper is organized as follows: Section 2 presents materials and methods. Section 3 presents the results of the validation approach, demonstrating the performance of the proposed framework in product advertising settings using a pilot robot-mediated experiment, while Section 4 discusses the results. Then, conclusions follow.

2 Materials and Methods

This section presents a BCI framework that uses derivative-based similarity metrics to characterize EEG spatiotemporal dynamics. The framework is validated through its application in a neuromarketing context and is specifically designed for real-time consumer choice prediction and seamless integration within social robots.

2.1 Participants

Nine healthy participants with an average age of 33 years (minimum 21, maximum 59) took part in the study. The study was approved by the Ethics Committee of the Institute of Robotics, BAS (Protocol №5/24.09.2024). Before participation, each participant signed an informed consent form.

2.2 Materials

2.2.1 Hardware

We use OpenBCI Cyton + Daisy biosensing boards (16-Channels) for collecting EEG signals. For stimuli presentation, we used the Furhat social robot, which has a back-projected, customizable human face, two microphones and speakers, along with a connected tablet, which exchanges events with Furhat's skills, enabling asynchronous, event-driven interactions. Furhat's ability to speak in natural language, maintain eye contact, display facial gestures, and track user attention makes it suitable for administering neuromarketing stimuli in the study.

2.2.2 Software

To facilitate integration among the BCI device, the robot, and cloud services, the Node-RED platform, which provides an intuitive graphical interface for visual programming, is used. The Node-RED nodes from the OpenBCI toolkit were used to interface with BrainFlow-supported BCI devices. How EEG data streams can be configured, featured, and controlled via visual workflows is described in detail in [9].

Furhat skill was programmed using Furhat SDK, which utilizes a Domain-Specific Language (DSL) implemented in Kotlin. The skill integrates a React-based graphical user interface via the *furhat-gui* library to manage the robot's GUI behavior.

2.2.3 Set-up and Stimuli Description

To elicit brain responses, a web application administered by the Furhat robot was used to present images of different products to participants, who could respond with "Like", "Dislike", and "Buy" (Figure 1).

We used five distinct items as stimuli, each presented with the baseline product, the product with a discount (promotion stimuli), and the product with endorsement stimuli. Product endorsement is a marketing communication tool intended to positively influence consumer perception, whereas sales promotion is a technique in which marketers provide discounts or cashback to encourage purchase behavior. The protocol for stimulus

sequence and timing was implemented as described in [7], and presented in Figure 2.

Fig. 1: Experimental set-up
Source: Created by the authors

Fig. 2: A protocol for stimulus sequence and timing
Source: Created by the authors

2.2.4 Data Collection

EEG data were acquired at a sampling rate of 125 Hz using the OpenBCI Cyton + Daisy system, which is defined as a board name in the node "open-BCI Streaming" from the Node-RED openBCI toolkit. It provides access to the raw data from the EEG device board. In line with [6], [7], [8], electrodes of interest are: AF3, AF4, F3, F4, F7, F8, FC5, FC6, Cz, Pz, P3, and P4. The activity of brain signals in microvolts is recorded from the moment the marketing product is visualized until the participant selects a response. The resulting EEG activity from specific brain regions is recorded in the Node-RED internal memory for online or offline analysis.

2.3 Methods

This subsection first describes the method used to synchronize the selection of items, as registered by Furhat events, with the recording of raw EEG data. Next, the methods for preprocessing the raw EEG data are described, including normalization, feature extraction, classification procedures, and the performance metrics used for data analysis.

2.3.1 Data Collection

A new software integration and synchronization method is proposed for collecting consumer choice data by integrating the OpenBCI system with the Furhat robot using the Node-RED platform. The method enables communication among the OpenBCI device, the robot, and a tablet or voice interface, supporting real-time data acquisition, signal processing, and seamless system synchronization. This integration allows full analysis of participants' brain activity in relation to their preferences and reactions (Figure 3).

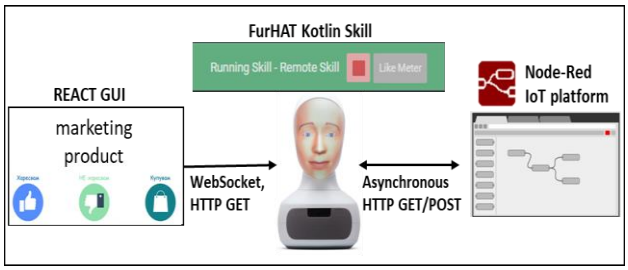

Fig. 3: Integration and synchronization of OpenBCI and Furhat software
Source: Created by the authors

The developed custom Furhat skill integrates a React-based GUI to present marketing surveys with three possible responses. Bidirectional, real-time communication between the user's browser and the Furhat server is achieved through a custom API and the *furhat-gui* library. The WebSocket protocol provides event-based communication, enabling the GUI to receive events from the Furhat skill and send responses back. For real-time synchronization of stimulus presentation and user interaction, either verbally or via tablet, a custom API was developed to enable bidirectional communication between the user application and the Furhat server. The connection between Furhat and Node-RED was established using the "*Receive from Furhat*" node, which relies on an HTTP POST request via the "*http in*" node.

To align Furhat-generated events with recorded EEG data, a novel synchronization method was implemented to ensure that each stimulus presented by Furhat is identifiable throughout its duration within the EEG recordings. Furhat events are asynchronously logged with timestamps in a local JSON file, which is subsequently read by a Node-RED node to temporally align events with the EEG stream. This approach supports asynchronous data exchange between Furhat and the EEG streaming node while preserving all events for post-hoc analysis.

The synchronization workflow is initiated by the "Receive from Furhat" node. The complete Node-RED flow for EEG data registering, processing, and synchronizing events registered by Furhat with the recorded EEG data is illustrated in Figure 4.

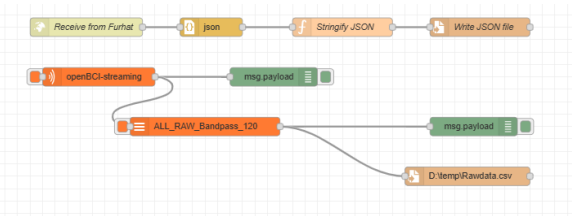

Fig. 4: Node-RED flow to synchronize events registered by Furhat with the recorded EEG data
Source: Created by the authors

2.3.2 Data Processing

Raw EEG signals were first preprocessed in Node-RED using standard filtering procedures - a bandpass filter (0.5–40 Hz) was applied to remove DC drift, low-frequency offsets, muscle artifacts, and high-frequency electrical noise, while a notch filter was used to suppress power-line interference. After filtering, EEG signals were normalized using z-score normalization to ensure comparability across channels and participants. The normalization parameters, mean (μ) and standard deviation (σ), were derived not during a beginning calibration phase, but during the session from the first three intervals (each 5-seconds) between two "Until answer" blocks (see the Timeline in Figure 2). The data were then segmented into stimulus-locked blocks using preference labels corresponding to the stimuli presented by the social robot and transmitted to the BCI flow in Node-RED. For each trial, EEG samples were extracted between stimulus onset and offset and assigned behavioral labels of "Like", "Dislike", and "Buy". Each EEG sample x, z-normalized by $y=(x-\mu)/\sigma$, has a value close to 0 when the brain activity is near the calibration mean, a value around ±1 corresponds to approximately one standard deviation from the mean, and a value around ±2 represents approximately two standard deviations from the mean. All stimulus-locked segments (subsets) were concatenated into a single dataset to enable signal averaging and cross-participant analysis.

2.3.3 Feature extraction and Classification

The feature extraction is based on time–frequency band power analysis aligned to stimulus onset in moving windows. Window sizes were selected based on a trade-off between temporal and frequency resolution. For theta (4–8 Hz) and alpha (8–12 Hz) bands, 0.5 s windows (62 samples) were used, while for beta (16–25 Hz) and gamma (25–40 Hz) bands, shorter 0.25 s windows (31 samples) were applied. Band power was computed separately for each frequency band and channel, using segmented stimulus-specific subsets corresponding to the "Like", "Dislike", and "Buy" conditions.

Power spectral density was estimated using Welch's method. To capture temporal dynamics, first- and second-order derivatives of band power were calculated in overlapping windows. The first-order derivative quantified the rate of change in spectral power over time $P(t)$ following stimulus presentation, while the second-order derivative reflected the acceleration of power changes, capturing sudden dynamics and nonstationary neural responses to the stimuli. While average power and first-order derivatives may show similar patterns across stimuli, second-order derivatives expose evident distinctions in dynamic patterns between the stimuli (Figure 5).

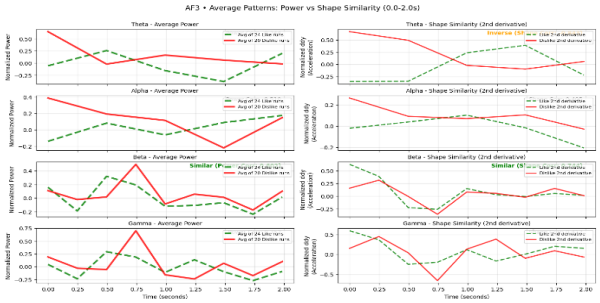

a. Average spectral power vs shape similarity for AF3

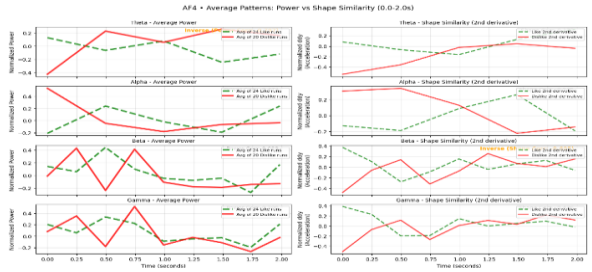

b. Average spectral power vs shape similarity for AF4

Fig. 5: Average power versus second-order derivative analysis showing improved discrimination between stimuli
Source: Created by the authors

The analysis of features was restricted to the 0.5–2 s post-stimulus interval, which aligns with the early decision-making phase. The analysis of similarity was first conducted using descriptive statistics, followed by evaluation with Cohen's d and CIs to assess the magnitude and reliability of differences across stimuli. We started with examination of kurtosis and skewness, where negative skewness indicated more frequent strong

downward curvatures (the peaks of interest), while positive skewness reflected more evident upward curvatures, and in this context, skewness aligns more closely with the sign behavior of the second derivative than kurtosis. However, these statistics cannot assess similarity or dissimilarity between spatiotemporal EEG patterns across stimuli, as kurtosis and skewness are scalar windowed descriptors that capture only local signal characteristics. We then examined Pearson correlation, Dynamic Time Warping (DTW), and cosine similarity computed on the second derivatives of band power in sliding windows. Pearson correlation and cosine similarity presume that the signals remain approximately stationary within each window; EEG signals typically exhibit nonstationary dynamics. To satisfy this assumption, the analysis window must therefore be sufficiently short to approximate local stationarity. We used a 500-ms sliding Hann window with 50% overlap, widely used and consistent with [3]. To further capture the fast neural dynamics, our analyses are based on time derivatives of the spectral power per band and channel ($y''=d^2P/dt^2$), thus emphasizing fast amplitude changes and transient temporal variations to reveal neural structures invisible in the raw EEG data.

DTW revealed that the temporal shapes of the "Like" and "Dislike" conditions were highly similar across most scalp regions, with similarity values close to 1.0 in the 0.5–2 s time window. This is probably because DTW emphasizes temporal alignment between time series, rather than differences in local dynamics, making it less suitable for capturing impulsive decision-related processes. Good discrimination was obtained using Pearson correlation-based shape similarity and cosine similarity computed on the second-order derivatives of band power, with results showing largely consistent patterns across the two measures (Figure 6). We therefore recommend Pearson correlation (1) for impulsive decision-making analyses due to its lower computational complexity.

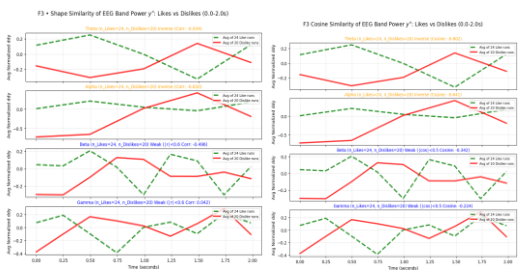

Fig. 6: Pearson correlation-based shape similarity and cosine similarity for channel F3
Source: Created by the authors

Equation (1) defines the proposed neuromarker: the Pearson correlation. $r_k$within window k of second derivatives of EEG power across frequency bands and channels, computed in sliding windows over the impulsive reaction interval (0.5-2.0s), quantifying differences in spatiotemporal power dynamics between stimuli through the similarity of their temporal curvature. Let $y_1''(t)$ and $y_2''(t)$ denote the second derivatives of spectral power per band for two stimuli, w denote the window length (in seconds), and k denote the start index of the sliding window.

$$r_k = \frac{\sum_{t=k}^{k+w}\left(y_1''(t)-\overline{y_1''}_k\right)\left(y_2''(t)-\overline{y_2''}_k\right)}{\sqrt{\sum_{t=k}^{k+w}\left(y_1''(t)-\overline{y_1''}_k\right)^2}\sqrt{\sum_{t=k}^{k+w}\left(y_2''(t)-\overline{y_2''}_k\right)^2}} \quad (1)$$

where:

$$\overline{y_1''}_k = \frac{1}{w}\sum_{t=k}^{k+w} y_1''(t), \overline{y_2''}_k = \frac{1}{w}\sum_{t=k}^{k+w} y_2''(t) \quad (2)$$

are the mean second-order values within window k.

Cohen's d (3) is computed from the standardized mean difference between conditions, using pooled variance estimates across trials. Confidence intervals are derived from the standard error of the effect size to assess statistical reliability. Equation (5) its 95% CI across bands and channels.

$$d = \frac{\mu_1-\mu_2}{s_p} \quad (3)$$

where:
μ_1 - mean of a feature extracted from stimulus 1 (e.g., mean $y_1''(t)$within window k)
μ_2 - mean of the same feature for stimulus 2
s_1^2, s_2^2 - corresponding sample variances
n_1, n_2 - number of trials per condition
s_p - pooled standard deviation

$$s_p = \sqrt{\frac{(n_1-1)s_1^2+(n_2-1)s_2^2}{n_1+n_2-2}}$$

Equation (4) defines the standard error of Cohen's d.

$$SE_d = \sqrt{\frac{n_1+n_2}{n_1 n_2}+\frac{d^2}{2(n_1+n_2)}} \quad (4)$$

Equation (5) defines the 95% confidence interval.

$$CI_{95\%} = d \pm 1.96 \cdot SE_d \quad (5)$$

2.3.4 Data Analysis

For the present study, a custom Python-based environment for higher-order statistical descriptors and similarity metrics of EEG data analysis was developed. The *scipy.stats* module was employed to

perform Pearson correlation analysis (*pearsonr*), as well as higher-order statistical descriptors, such as kurtosis and skewness, to characterize the distributional properties of EEG signals. The *dtaidistance.dtw* module was employed for DTW to compare EEG time series that may be temporally misaligned, while the *sklearn.metrics.pairwise.cosine_similarity* module was employed for cosine similarity to quantify the similarity between EEG feature vectors, facilitating the comparison of spatial and temporal patterns across experimental conditions.

Comparing the second derivatives of band power between two stimuli (S1 and S2) captures differences in power acceleration over time. Stimuli are considered discriminable when their temporal dynamics are weakly or negatively correlated - low Pearson r indicates uncorrelated dynamics, while negative r reflects inverse temporal structure, highlighting stronger differentiation in neural processes. A threshold of r ≥ -0.6 was selected based on conventional correlation guidelines, where values ≥ 0.6 are typically interpreted as large effect sizes, [10]. Given the inherent variability of EEG signals, a cosine similarity threshold of > 0.5 was selected (corresponding to an angle < 60°), indicating substantial directional alignment between signals, which are commonly interpreted as reflecting meaningful pattern similarity.

3 Results

As we mentioned above, the Pearson correlation-based shape similarity and the cosine similarity of the second derivatives of averaged band-limited frequency power for different stimuli in the 0.5–2.0 s time window are generally consistent. The channels that are not inversely similar mostly appear among the three weakest channels (Table 1). Therefore, due to its lower computational complexity, we will discuss only the Pearson correlation results for "Like" versus "Dislike" decisions.

3.1 Shape Similarity between "Like" and "Dislike" in the First 2 s after Stimuli

We compared the average spatiotemporal EEG dynamics for "Like" and "Dislike" decisions across theta, alpha, beta, and gamma frequency bands using Equation (1). Electrodes showing strong inverse correlations ($r \geq -0.6$) were interpreted as important neuromarkers for impulsive consumer choices.

Table 1. Comparison of Pearson correlation and cosine similarity of second-order spectral power across channels and bands, highlighting inversely similar and weak channels (0.5–2.0 sec window)

Band	Inverse channels		Weak channels (first 3)	
	Pearson r ≤ -0.6	**Cosine ≤ -0.5**	**Pearson r**	**Cosine**
Theta	AF3:-0.975 F3:-0.934 C3:-0.870 AF4:-0.810 Pz:-0.743 P4:-0.697	F3:-0.802 AF3:-0.78 F8:-0.726 P4:-0.646 C3:-0.636 T7:-0.624 T8: -0.623	T8:-0.557 T7:-0.527 F7: -0.289	Pz:-0.27 AF4: -0.09 F4: 0.105
Alpha	C3: -0.959 F8: -0.959 P3: -0.929 F3: -0.830 AF4:-0.783 C4: -0.697	C3:-0.912 F8:-0.784 Cz:-0.692 F3: -0.641 AF4:-0.56	P4: -0.183 AF3:-0.17 O1: 0.347	P3:-0.37 C4:-0.022 AF3: 0.131
Beta	AF4:-0.693	O1:-0.737 AF4: -0.617	O1: -0.598 F3: -0.496 P4: -0.391	T7:-0.422 F3:-0.342 F7:-0.121
Gamma	O2: -0.693	O2: -0.572	O1: -0.489 Cz: -0.453 F4: -0.356	C3:-0.492 Cz:-0.480 F4:-0.407

Source: Created by the authors

3.1.1 Theta Band (4–8 Hz)

In the theta band, strong inverse temporal patterns between conditions were observed predominantly over prefrontal, frontal, and parietal regions (Figure 7). The strongest inverse correlations occurred at AF3, F3, C3, AF4, Pz, and P4.

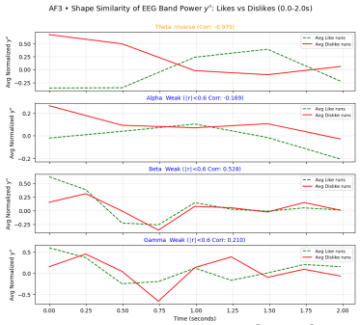

a. AF3: Shape Similarity of d^2P/dt^2 across bands

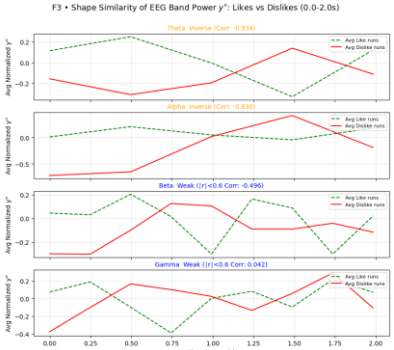

b. F3: Shape Similarity of d2P/dt2 across bands

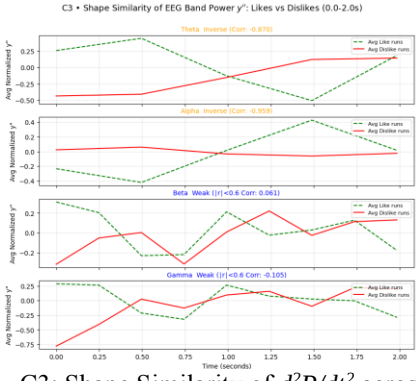

c. C3: Shape Similarity of d^2P/dt^2 across bands

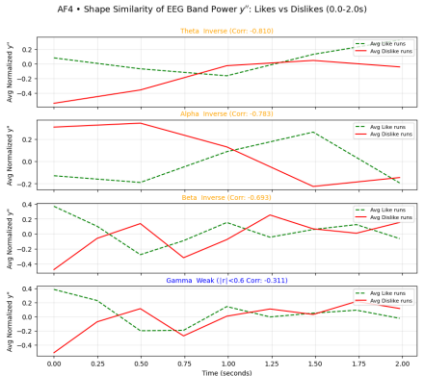

d. AF4: Shape Similarity of d^2P/dt^2 across bands

e. Pz: Shape Similarity of d^2P/dt^2 across bands

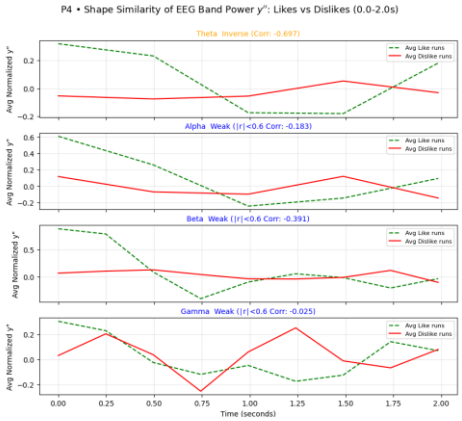

f. P4: Shape Similarity of d^2P/dt^2 across bands

Fig. 7: Strongest discriminative patterns between "Like" and "Dislike" conditions at AF3, F3, C3, AF4, Pz, and P4

Source: Created by the authors

High positive similarity was observed at central and occipital electrodes (Cz, O1, O2, P3), suggesting that both stimuli elicited similar patterns of sensory processing and midline activation.

3.1.2 Alpha Band (8–12 Hz)

Alpha-band activity also demonstrated strong discriminative effects across frontal and parietal sites. Strong inverse correlations were observed at C3, F8, P3, F3, AF4 and C4 (Table 1). In contrast, high similarity was observed at temporal, occipital, and central sites T7, O2, Cz, and T8.

3.1.3 Beta Band (13–30 Hz)

Beta-band dynamics were largely similar between conditions, particularly over central and parietal regions: Cz, Pz, C4, T8, and P3. A single electrode, AF4, exhibited an inverse pattern, indicating a localized prefrontal activation to discriminate affective preference.

3.1.4 Gamma Band (30–40 Hz)

An inverse temporal pattern was observed at the right occipital electrode O2, while the remaining ten electrodes showed weak correlations or four nonsignificant correlations.

3.1.5. Cohen's d and 95% Confidence Intervals between "Like" and "Dislike" Conditions

To provide a complementary distribution-level measure of effect magnitude and direction, we calculated Cohen's *d* (3) and corresponding 95% CIs (5) for the "Like" versus "Dislike" across all electrodes and frequency bands within the first 2 s following stimulus onset. Unlike the Pearson correlation of second derivatives, which quantifies dynamic waveform similarity or inversion, Cohen's *d* (3) evaluates the magnitude and stability of mean separation between conditions across trials. We then integrated the derivative-based dynamic analysis with confidence-interval-validated effect sizes to obtain a consolidated representation of both temporal structural reorganization and distribution-level neural differentiation. The resulting consolidated summary is presented in Table 2.

The strongest polarity-dependent effects emerged in the theta band, where several electrodes showed large and statistically reliable separations between conditions. F8 exhibited the largest "Like" dominant response ($d = 1.27$, 95% CI fully above zero), followed closely by T8 ($d = 1.11$) and AF4 ($d = 1.10$), both reflecting robust right-temporal and frontal "Like" dominant activity. In contrast, Pz showed a strong "Dislike" dominant pattern ($d = -1.17$, CI fully below zero), indicating reliable

parietal differentiation. Within the alpha band, AF3 demonstrated a pronounced "Dislike" dominant effect (d = -1.09, CI fully negative), highlighting left-frontal suppression during "Like" evaluations.

Table 2. Consolidated summary of channel convergence, where the strongest support is indicated by combined evidence from significant Pearson correlations and effect sizes whose 95% CIs exclude zero

Band	**Type of Evidence**	**Channels**	**Effect Sizes |d| ≥ 0.60 and 95% CI excludes 0**
Theta (Overlap 83%)	Pearson correlation only	C3	-
	Effect-only	F8, T8, Cz, F7, T7	F8: 1.27 (0.62–1.92); T8: 1.11 (0.47–1.75); Cz: 0.84 (0.22–1.46); F7: 0.73 (0.12–1.34); T7: –0.66 (–1.27 to –0.06)
	Consolidation	AF3, F3, AF4, Pz, P4	AF3: –0.81 (–1.43 to –0.19); F3: 0.81 (0.19–1.42); AF4: 1.10 (0.46–1.73); Pz: –1.17 (–1.82 to –0.53); P4: 0.63 (0.03–1.24)
Alpha (Overlap ≈ 33%)	Pearson-only	P3, C3, F8, AF4, C4, Cz, O2, O1	-
	Effect-only	AF3, F7	AF3: –1.09 (–1.73 to –0.46); F7: 0.61 (0.00–1.22)
	Consolidation	F3, Pz, T8, T7	F3: 0.89 (0.27–1.51); Pz: 0.77 (0.16–1.39); T8: 0.65 (0.04–1.26); T7: –0.61 (–1.22 to –0.01)
Beta (Overlap 50%)	Pearson-only	P3, AF4	-
	Effect-only	T7	–0.64 (–1.25 to –0.03)
	Consolidation	Cz, Pz	Cz: –0.65 (–1.26 to –0.04); Pz: –0.61 (–1.22 to –0.01)

Source: Created by the authors.

Although gamma-band electrode O2 confirmed inverse derivative-based dynamics, it did not meet the combined effect-size robustness criterion (|d| ≥ 0.60 with CI excluding zero), indicating that dynamic curvature differences were not supplemented by stable distribution-level separability across trials.

3.2 Buy-endorsement vs Buy-discount

It is important to note a limitation when comparing averaged responses for "Buy" (endorsement vs discount) conditions. Across all participants, only four instances of purchases were linked with the discount condition and three with the endorsement condition. Therefore, these results require further validation through additional experiments with larger and more balanced samples.

3.2.1 Theta Band (4–8 Hz)

The strongest discriminative effects between "Endorsement" and "Discount" conditions were observed outside the frontal cortex. Very strong inverse patterns were observed at O2 (r=-0.935), O1 (r=-0.887), and Cz (r=-0.837), suggesting oppositely structured theta-band dynamics across conditions. These effects are consistent with differential visual–attentional processing in occipital regions (O1/O2) and distinct decision-related or action-preparatory processes reflected at the central midline (Cz). In contrast, frontal electrodes exhibited weak or highly similar theta dynamics across conditions.

3.2.2 Alpha Band (8–12 Hz)

Alpha-band activity showed robust and lateralized discriminative effects, with strong inverse correlations at C4 (r =-0.987) and AF4 (r =-0.97). These findings indicate strong right-hemisphere dominance, reflecting differences in frontal inhibitory control and cognitive evaluation between Endorsement and Discount conditions.

3.2.3 Beta Band (13–30 Hz)

In the beta band, clear discrimination was observed, with strong inverse patterns at O2 (r = -0.917), F3 (r = -0.859), and P3 (r = -0.732). This pattern suggests condition-specific differences in visual decision certainty and left frontal executive control.

3.2.4 Gamma Band (30–40 Hz)

A strong inverse pattern was observed at Pz (r = -0.836), F4 (r = -0.784), and O1 (r = -0.644). These findings indicate that right frontal gamma activity is particularly sensitive to social versus price-driven motivational processes, consistent with the broader role of the posterior parietal cortex in guiding attention and decision behavior.

3.2.5 Cohen's d and 95% CIs between "Endorsement" and "Discount" Conditions

Due to the limitation mentioned earlier, we did not provide a complementary distribution-level measure

of effect size and direction when comparing averaged responses for "Buy". However, this can be computed analogously using Equations (3)-(5).

4 Discussion

The obtained results indicated that neuromarketing-related EEG differences are mainly in the spatiotemporal dynamics of brain activity, rather than in static metrics of absolute or relative power. The observed inverse dynamics indicate that "Like" and "Dislike" impulsive decisions engage oppositely structured neural state transitions and can therefore serve as a neuromarker for dynamic, stimulus-based discrimination. Furthermore, in neuromarketing, social robots could serve as interactive interfaces to BCI systems, helping to overcome the major challenge of EEG signal interpretability by providing real-time explanations and feedback during consumer choice prediction. Standard EEG outputs require specialized neuroscientific expertise to decode, which limits accessibility for non-expert users. Integrating LLMs into social robots to translate EEG activity in real time, i.e., from 'waves' to 'words', can simplify interpretation. For example, a robot can provide explanatory feedback by indicating that the strongest discriminative inverse patterns were observed in the theta band at AF3, and that this finding is theoretically grounded in frontal theta mechanisms associated with negative valence and the neural processing of dislike-related evaluations. Similarly, a refined LLM to use the proposed second-order (d^2y/dt^2) metric per bands and channels, the robot can say: "I found that the neural patterns distinguishing 'Like' versus 'Dislike' decisions are strongly lateralized, reflecting distinct temporal dynamics across the two hemispheres. This aligns with [7], who found that bilateral frontal electrodes, particularly AF3/AF4, F3/F4, and F7/F8, are most informative for affective and purchase-related decisions, supporting a right-hemisphere specialization for processing negative or aversive responses.

4.1 Discriminative EEG Spatiotemporal Dynamics Underlying "Like" and "Dislike"

Table 1 presents the most strongly discriminative inverse patterns, where the second-order dynamics for "Like" and "Dislike" decisions were nearly exact opposites, observed in the theta band at AF3 (-0.975) and F3 (-0.934), and in the alpha band at C3 (-0.959), F8 (-0.959) and P3 (-0.929). Overall, the theta and alpha bands are the strongest discriminators, showing the highest number of informative channels (6 out of 16), indicating highly polarized spatiotemporal dynamics between conditions. The observed theta patterns in our data, especially at prefrontal and frontal sites F3, AF3, and F8, align with [11], [12], [13], who reported modulation by negative or aversive stimuli and engagement of cognitive control by negative outcomes. Concerning alpha activity, the results indicate that emotional valence modulates alpha activity, with the strongest effects observed at central-parietal sites (C3: -0.959; P3: -0.929), followed by frontal sites (F8: -0.959; F3: -0.830; AF4: -0.783). Our findings align with [14], where it is reported that viewing emotional (positive or negative) images, compared with neutral ones, consistently elicits increased alpha desynchronization over posterior sensors, reflecting a decrease in alpha power. Consistent with [15], inverse oscillatory patterns (e.g., alpha ERD vs. ERS) reflect differential engagement: ERD indicates increased task-relevant processing, while ERS marks reduced activity, observed at frontal and prefrontal sites during top-down control tasks, part of which are evaluating products or making purchase choices.

Furthermore, neuromarketing and BCI research in [7], consistently identified bilateral frontal electrodes as the most informative sites for affective and purchase-related decisions. Particularly, electrodes AF3/AF4, F3/F4, and F7/F8 play a central role in encoding Affective Attitude (AA) and Positive Purchase Intention (PPI). The highest classification performance for positive AA ("Like") was achieved when all six frontal channels (AF3, AF4, F3, F4, F7, F8) were combined, reaching 87% accuracy, confirming these regions as maximally engaged during liking responses. Similarly, PPI classification peaked at 84% accuracy using the same frontal channels, while the best-performing electrode pair was F3 + F4 (81.5%), highlighting the importance of bilateral frontal integration during PPI. In terms of spectral features, *theta (4–8 Hz)* emerged as the dominant band, followed by delta (0–4 Hz), followed by low beta and high beta, reflecting combined cognitive control and emotional valuation processes. According to [7], both AA conditions recruit the same frontal network; however differ in signal dynamics rather than spatial localization. Dislike responses exhibit greater variability and dispersion, particularly at AF3, along with pronounced N200 ERP components, indicating faster and stronger neural reactions to negative stimuli. Together, these findings suggest that frontal

electrodes encode affective preference through distinct temporal and dynamic EEG patterns.

Concerning beta-band activity, the strongest discriminative inverse patterns were observed at O1, associated with emotional visual processing, and AF4 (right-frontal), linked to emotional/cognitive conflict and avoidance tendencies. Several studies have shown that emotionally salient or aversive images modulate beta power in occipital regions, typically interpreted as reflecting visual-cortical processing differences or increased attention to emotional stimuli, [16], [17], reported that emotional pictures produce increased beta desynchronization in posterior regions, reflecting enhanced visual processing.

Concerning gamma-band activity, high-gamma EEG is sensitive to differences in emotional states and can differentiate positive, neutral, and negative emotion processing across distributed networks, including occipital regions, [18]. Invasive EEG evidence further shows that occipital high-gamma activity is modulated by emotional picture processing, particularly distinguishing affective from neutral stimuli in the visual cortices, [19]. Although Pearson similarity, gamma-band activity did not satisfy the effect-size stability criterion, since the mean difference between "Like" and "Dislike" was negligible (d = -0.055) and the 95% CI (-0.649 to 0.538) included zero, there was no statistically reliable separation between conditions despite observable dynamic differences.

Convergent analysis across derivative-based shape similarity and effect-size inference identified AF3, F3, AF4, Pz, and P4 as the most robust polarity-sensitive theta electrodes. All five electrodes demonstrated both structural temporal dynamics and statistically reliable mean separation, with CIs excluding zero. Effect sizes were large at AF3 (d = -0.81, 95% CI: -1.43 to –0.19), F3 (d = 0.81, 95% CI: 0.19-1.42), AF4 (d = 1.10, 95% CI: 0.46-1.73), and Pz (d = -1.17, 95% CI: -1.82 to -0.53), while P4 showed a moderate but reliable effect (d = 0.63, 95% CI: 0.03–1.24). The spatial distribution, spanning bilateral frontal (AF3, F3, AF4) and parietal regions (Pz, P4), suggests that theta-band polarity encoding is mediated by a distributed fronto-parietal network. The convergence of dynamic inversion (derivative similarity) and distribution-level stability (effect size with non-zero CI) indicates that theta curvature dynamics provide the strongest and most consistent neural marker of evaluative polarity in this framework. In the alpha band, F3 (d = 0.89, 95% CI: 0.27-1.51), Pz (d = 0.77, 95% CI: 0.16-1.39), T8 (d = 0.65, 95% CI: 0.04-1.26), and T7 (d = -0.61, 95% CI: -1.22 to -0.01) demonstrated consistent structural and distribution-level differentiation. In the beta band, Cz (d = -0.65, 95% CI: -1.26 to -0.04) and Pz (d = -0.61, 95% CI: -1.22 to -0.01) showed moderate but statistically reliable effects. Particularly, Pz and F3 exhibited cross-band stability, suggesting distributed fronto-parietal involvement in polarity encoding. These findings indicate that while theta band effects were strongest overall, alpha and beta bands contribute complementary and statistically robust polarity-sensitive dynamics.

4.2 Discriminative EEG Spatiotemporal Dynamics Underlying Discount- and Endorsement-Driven Purchase Decisions

Again, we note the limitation when comparing averaged responses for "Buy" conditions, as the sample contained only seven purchase instances in total (four under the discount condition and three under the endorsement condition), which may limit statistical generalization. The discrimination between discount-based and endorsement-based purchase decisions was particularly evident in right frontal gamma activity and occipital regions associated with attention-related dynamics. These patterns suggest that the two decision contexts engage distinct motivational and valuation strategies, rather than merely differing in stimulus intensity.

We found strong discrimination between endorsement and discount conditions, reflected in inverse shape patterns, observed for theta at O2, O1, Cz, and alpha with $r \sim -0.98$ at C4 and AF4. The comparison between endorsement-based and discount-based purchase decisions revealed marked differences in neural dynamics, particularly at the occipital site O1/O2 (Figure 8). The key finding was the presence of very high inverse shape patterns in both the theta and alpha bands, indicating opposite temporal trajectories between the two choice conditions. In the theta band, endorsement and discount choices followed mirror-opposed trajectories across the decision window, suggesting divergent engagement of cognitive control and evaluative processes. Theta activity is commonly associated with effortful decision-making and conflict monitoring; thus, the inverse pattern implies that endorsement-based choices may rely on internally driven evaluative mechanisms (e.g., trust, social validation), whereas discount-based choices engage more externally driven, incentive-based processing. Similarly, alpha activity at C4 and AF4

exhibited a strong inverse relationship between conditions. Alpha desynchronization is typically associated with enhanced attentional engagement and task-relevant processing. The opposing alpha trajectories therefore suggest differential allocation of attentional resources, with endorsement decisions potentially eliciting more sustained evaluative processing, whereas discount decisions may rely on faster or more heuristic mechanisms driven by salient price information. In the beta band, clear discrimination between conditions was observed, with strong inverse patterns at O2 (r = -0.917), F3 (r =-0.859), and P3 (r=-0.732). Beta activity in occipital and parietal regions has been linked to visual processing and decision confidence, while left frontal beta is commonly associated with executive control and goal-directed behavior. The opposing beta dynamics across these sites therefore suggest condition-specific differences in visual decision certainty and top–down executive engagement during the evaluation process. In the gamma band, strong inverse patterns were detected at Pz (r=-0.836), F4 (r =-0.784), and O1 (r =-0.644). Gamma activity in right frontal regions has been associated with motivational and affective integration, while parietal gamma is broadly implicated in attentional control and decision-related integration. Together, these findings suggest that gamma-band dynamics are sensitive to differences between social and price-driven motivational processes, consistent with the established role of frontoparietal networks in guiding attention and decision behavior.

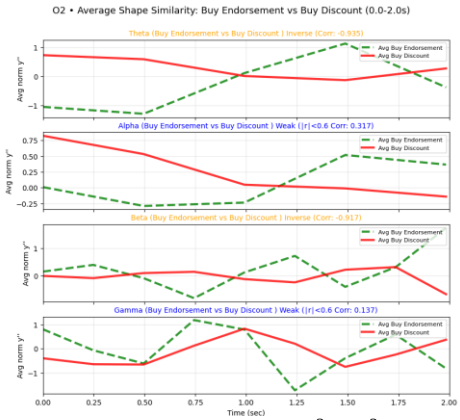

a. O2: Shape Similarity of d^2P/dt^2 across bands

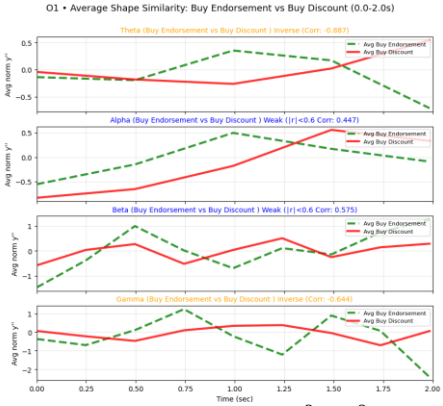

b. O1: Shape Similarity of d^2P/dt^2 across bands

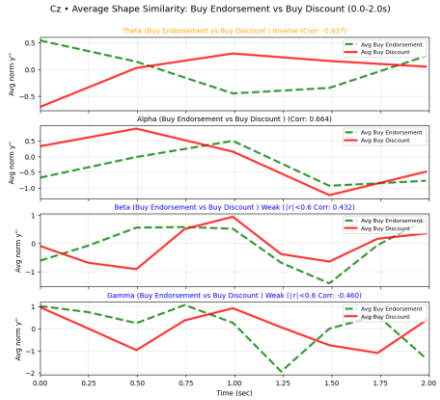

c. Cz: Shape Similarity of d^2P/dt^2 across bands

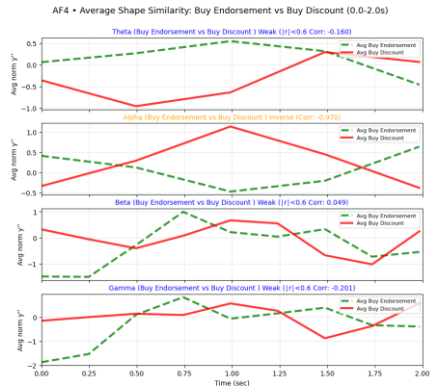

d. AF4: Shape Similarity of d^2P/dt^2 across bands

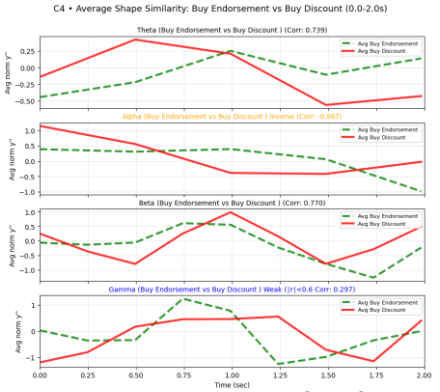

e. C4: Shape Similarity of d^2P/dt^2 across bands

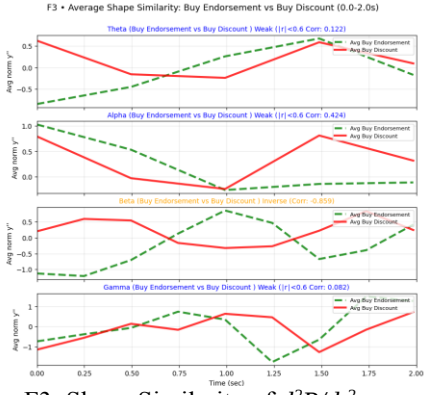

f. F3: Shape Similarity of d^2P/dt^2 across bands

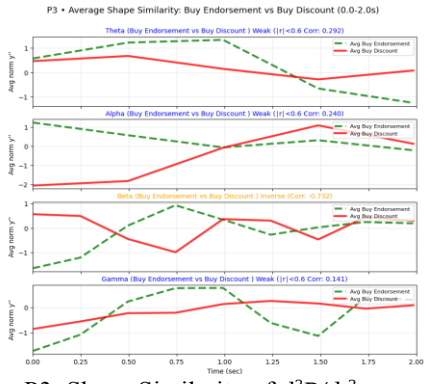

g. P3: Shape Similarity of d^2P/dt^2 across bands

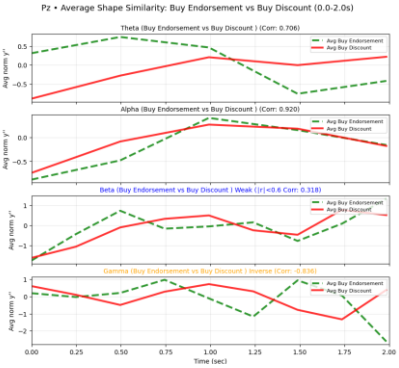

h. Pz: Shape Similarity of d^2P/dt^2 across bands

Fig. 8: Strongest inverse correlations for "Buy" (endorsement vs discount) at O2, O1, and Cz in theta; AF4 and C4 in alpha; O2, F3, and P3 in beta; Pz and O1 in gamma
Source: Created by the authors

In the neuromarketing context, endorsement-driven decisions are known to catch social influence and affective processing systems, a finding consistently reported across neuromarketing EEG studies. Systematic reviews of EEG neuromarketing research, [20], show that emotionally and socially rich messages reliably modulate frontal EEG markers and predict preference and purchase intention. More directly, recent EEG experiments comparing human and virtual influencers, [21], demonstrate that endorsement contexts alter both behavioral purchase intentions and neural signatures, providing empirical evidence that endorsement cues reshape valuation processes at the neural level.

We found parietal gamma and right frontal gamma activity at Pz and F4 showed strong discrimination between endorsement and discount conditions. These findings support the interpretation that endorsement decisions recruit distinct high-frequency frontal mechanisms linked to evaluative depth and social relevance, whereas discount decisions rely more on shared, lower-frequency control processes. This is consistent with [22], linking frontal gamma oscillations and fronto-parietal gamma coupling to value-based decision-making, salience processing, and the rapid integration of affective information. Authors in [22], demonstrated that frontal gamma coupling predicts the accuracy of value-based choices, emphasizing the unique role of frontal regions in valuation. Consistent with [23], showing that frontal gamma power reflects emotional regulation and the representation of affective goals. Endorsements inherently carry social meaning and normative cues, which likely modulate affective goals differently from price reductions. Thus, the sensitivity of right frontal gamma to endorsement versus discount conditions plausibly reflects differential engagement of social-emotional valuation circuits, rather than general task difficulty or arousal.

Summarizing, frontal gamma effects likely reflect social-emotional valuation processes, whereby decisions are guided by credibility, social identification, or affective resonance with the endorser, consistent with the role of gamma oscillations in fast integrative neural communication.

In contrast, discount-based decisions appear to rely more strongly on price evaluation and visually grounded attention mechanisms, as reflected in the discriminative involvement of occipital electrodes (e.g., O1 and O2). EEG and MEG studies of price perception show that price cues elicit rapid neural responses associated with expectancy violation and value computation, often within occipital and parietal networks, [24]. These findings suggest that discounts trigger fast, stimulus-driven evaluation processes grounded in visual and numerical information. Supporting this view, studies of shopping-related attention demonstrate that visually driven cues, such as price tags and discounts, modulate occipital alpha and beta activity, reflecting attentional allocation and visual suppression mechanisms, [25]. Thus, discount conditions are likely processed through a more analytic and visually anchored decision strategy, emphasizing cost–benefit comparison rather than social meaning.

Even with limited data, the results point to distinct neural strategies underlying endorsement- and discount-based choices, most clearly reflected in theta and alpha activity. Inverse dynamics at posterior sites (e.g., O1 and O2) indicate distinct attentional and perceptual processing for endorsement- versus discount-based purchase decisions. These results are consistent with [20], [21].

5 Conclusions

This research introduces a real-time BCI framework that uncovers hidden emotional and impulsive choice responses using a computationally lightweight, derivative-similarity-driven spatiotemporal EEG analysis. To quantify similarity, we proposed a novel neuromarker based on the Pearson correlation of second-order derivatives of EEG power across frequency bands and channels, computed within sliding windows over the impulsive human reaction interval of 0.5–2.0s. We validated the first robot-mediated neuromarketing framework for real-time consumer choice prediction, distinguishing like, dislike, and purchase intentions during the early impulsive response in a social robot-driven advertising pilot study. Our findings demonstrate that the proposed neuromarker provides a computationally efficient framework for real-time analysis, while Cohen's *d* with CIs ensures statistical robustness by validating the stability and reliability of the observed condition differences.

Ongoing large-scale validation studies are needed to further contextualize these findings and address potential concerns regarding robustness by including a larger and more demographically and professionally diverse participant sample.

References:

[1] Lekova A., Chavdarov I.: A fuzzy shell for developing an interpretable BCI based on the spatiotemporal dynamics of the evoked oscillations. *Computational Intelligence and Neuroscience*, Vol. 2021, 2021, Article 6685672. https://doi.org/10.1155/2021/6685672.

[2] Ramon C., Gargiulo P.: Phase slips extracted from derivatives of EEG data provide a deeper insight into the formation of cortical phase transitions. *Frontiers in Integrative Neuroscience*, Vol. 19, 2025, Article 1471120. https://doi.org/10.3389/fnint.2025.1471120.

[3] Krukow P., Rodríguez-González V., Kopiś-Posiej N., Gómez C., Poza J.: Tracking EEG network dynamics through transitions between eyes-closed, eyes-open, and task states. *Scientific Reports*, Vol. 14, No. 1, 2024, Article 17442. https://doi.org/10.1038/s41598-024-68532-2.

[4] Šverko Z., Vrankić M., Vlahinić S., Rogelj, P.: Complex Pearson Correlation Coefficient for EEG Connectivity Analysis. *Sensors*, Vol. 22, No. 4, 2022, Article 1477. https://doi.org/10.3390/s22041477.

[5] Freedberg M., Reeves J. A., Hussain S. J., Zaghloul K. A., Wassermann E. M: Identifying site- and stimulation-specific TMS-evoked EEG potentials using a quantitative cosine similarity metric. *PLoS One*, Vol. 15, No. 1, 2020, Article e0216185. https://doi.org/10.1371/journal.pone.0216185.

[6] Golnar-Nik P., Farashi S., Safari M.: The application of EEG power for the prediction and interpretation of consumer decision-making: A neuromarketing study. *Physiology & Behavior*, Vol. 50, 2019, pp. 90-98. https://doi.org/10.1016/j.physbeh.2019.04.025

[7] Mashrur F., Rahman K., Miya M., Vaidyanathan R., Anwar S. F., Sarker F., Mamun K. A.: BCI-Based Consumers' Choice Prediction From EEG Signals: An Intelligent Neuromarketing Framework. *Frontiers in Human Neuroscience*, Vol. 16, 2022, Article 861270. https://doi.org/10.3389/fnhum.2022.861270.

[8] Gholami Doborjeh Z., Kasabov N., Gholami Doborjeh M., Sumich A.: Modelling Peri-Perceptual Brain Processes in a Deep Learning Spiking Neural Network Architecture. *Nature Scientific Reports*, Vol. 8, 2018, Article 8912. https://doi.org/10.1038/s41598-018-27169-8.

[9] Kremenska A., Lekova A., Kremenski S., Dimitrov G.: Validating the OpenBCI Nodes through EEG-based BCI Application for Smart Home Automation Control. *Journal of Communications Software and Systems*, Vol. 21, No. 3, 2025, pp. 250–261. https://doi.org/10.24138/jcomss-2025-0012.

[10] Cohen J.: Statistical Power Analysis for the Behavioral Sciences. ISBN: 9780805802832, Lawrence Erlbaum Associates, 1988, [Online]. https://www.taylorfrancis.com/books/mono/10.4324/9780203771587/statistical-power-analysis-behavioral-sciences-jacob-cohen (Accessed Date: January 1, 2026).

[11] Aftanas L. I., Varlamov A. A., Pavlov S. V., Makhnev V. P., Reva N. V.: Affective picture processing: event-related synchronization within individually defined human theta band is modulated by valence dimension. *Neuroscience Letters*, Vol. 303, No. 2, 2001, pp. 115–118. https://doi.org/10.1016/s0304-3940(01)01703-7.

[12] Aftanas L. I., Reva N. V., Varlamov A. A., Pavlov S. V., Makhnev V. P.: Analysis of evoked EEG synchronization and desynchronization in conditions of emotional activation in humans. *Neuroscience and Behavioral Physiology*, Vol. 34, 2004, pp. 859–867. https://doi.org/10.1023/B:NEAB.0000038139.39812.eb.

[13] Cavanagh J. F., Frank M. J.: Frontal theta as a mechanism for cognitive control. *Trends in Cognitive Sciences*, Vol. 18, No. 8, 2014, pp. 414–421. https://doi.org/10.1016/j.tics.2014.04.012.

[14] Codispoti M., De Cesarei A., Ferrari V.: Alpha-band oscillations and emotion: A review of studies on picture perception. *Psychophysiology*, Vol. 60, No. 12, 2023, Article e14438. https://doi.org/10.1111/psyp.14438.

[15] Benedek M., Bergner S., Könen, T., Fink A., Neubauer A. C.: EEG alpha synchronization is related to top-down processing in convergent and divergent thinking. *Neuropsychologia*, Vol. 49, No. 12, 2011, pp. 3505–3511. https://doi.org/10.1016/j.neuropsychologia.2011.09.004.

[16] Güntekin B., Başar E.: Event-related beta oscillations are affected by emotional eliciting stimuli. *Neuroscience Letters*, Vol. 483, No. 3, 2010, pp. 173–178. https://doi.org/10.1016/j.neulet.2010.08.002.

[17] Schubring D., Schupp H. T.: Affective picture processing: Alpha- and lower beta-band desynchronization reflects emotional arousal. *Psychophysiology*, Vol. 56, No. 8, 2019, Article e13386. https://doi.org/10.1111/psyp.13386.

[18] Yang K., Tong L., Shu J., Zhuang N., Yan B., Zeng Y.: High Gamma Band EEG Closely Related to Emotion: Evidence From Functional Network. *Frontiers in Human Neuroscience*, Vol. 14, 2020, Article 89. https://doi.org/10.3389/fnhum.2020.00089.

[19] Boucher O., D'Hondt F., Tremblay J., Lepore F., Lassonde M., Vannasing P., Bouthillier A., Nguyen D. K.: Spatiotemporal dynamics of affective picture processing revealed by intracranial high-gamma modulations. *Human Brain Mapping*, Vol. 36, No. 1, 2015, pp. 16–28. https://doi.org/10.1002/hbm.22609.

[20] Byrne A., Bonfiglio E., Rigby C., Edelstyn N.: A systematic review of the prediction of consumer preference using EEG measures and machine-learning in neuromarketing research. *Brain Informatics*, Vol. 9, No. 1, 2022, Article 27. https://doi.org/10.1186/s40708-022-00175-3.

[21] Yao Q., Liu Y., Jin J.: Virtual or Human Influencers as Endorsers? Behavioral and EEG Evidence of How Influencer Type Affects Purchase Intention of New Products. *Computers in Human Behavior*, Vol. 172, 2025, Article 108754. https://doi.org/10.1016/j.chb.2025.108754.

[22] Polanía R., Krajbich I., Grueschow M., Ruff C. C.: Neural oscillations and synchronization differentially support evidence accumulation in perceptual and value-based decision making. *Neuron*, Vol. 82, No. 3, 2014, pp. 709–720. https://doi.org/10.1016/j.neuron.2014.03.014.

[23] Kang J. H., Jeong J. W., Kim H. T., Kim S. H., Kim S. P.: Representation of cognitive reappraisal goals in frontal gamma oscillations. *PLoS One*, Vol. 9, No. 11, 2014, Article e113375. https://doi.org/10.1371/journal.pone.0113375.

[24] Gorin, A., Kuznetsova, E., Kislov, A., Levchenko E., Klucharev V., Moiseeva V., Yurchenko A, Luzhin A., Galkina N, Shestakova A.: Neural correlates of the non-optimal price: an MEG/EEG study. *Frontiers in Human Neuroscience*, Vol. 19, 2025, Article 1470662. https://doi.org/10.3389/fnhum.2025.1470662.

[25] Saffari F., Zarei S., Kakaria S., Bigné E., Bruni L. E., Ramsøy, T. Z.: The Role of Stimuli-Driven and Goal-Driven Attention in Shopping Decision-Making Behaviors-An EEG and VR Study. *Brain Sciences*, Vol. 13, No. 6, 2023, Article 928. https://doi.org/10.3390/brainsci13060928.

Contribution of individual authors to the creation of a scientific article (ghostwriting policy)

S. Kremenski: Project Administration. Data curation. Formal Analysis. Testing and refining the software. Writing - reviewing and editing
A. Lekova: Conceptualization and Methodology. Developing the statistical software framework. Writing - original draft, reviewing, and editing.
A. Kremenska: Exploring, developing, testing, and refining the software. Writing - reviewing and editing.

Sources of funding for research presented in a scientific article or scientific article itself

This research was funded by the EU Regional Development Fund under the OP "Scientific Research, Innovation and Digitization for Smart Transformation 2021–2027", Project CoC "Smart Mechatronics, Eco- and Energy Saving Systems and Technologies", BG16RFPR002-1.014-0005, and the equipment from the Bulgarian NSF, No. KP-06-H67/1.

Conflict of Interest

The authors have no conflicts of interest to declare that are relevant to the content of this article.

Creative Commons Attribution License 4.0 (Attribution 4.0 International, CC BY 4.0)

This article is published under the terms of the Creative Commons Attribution License 4.0
https://creativecommons.org/licenses/by/4.0/deed.en_US